The upsurge of absorption coefficient in $CuInS_2$ thin film with Ru doping: an energetic absorber layer in a superstrate solar cell

Logu Thirumalaisamy[a, *], Soundarrajan Palanivel[b], Karthikeyan Jeyakumar[c], Sethuraman Kunjithapatham[d, *], Trystan Watson[a], and Sudhagar Pitchaimuthu[e]

[a] SPECIFIC, Materials Research Centre, Faculty of Science and Engineering, Swansea University, Swansea, UK

[b] Department of Science and Humanities, Knowledge Institute of Technology (KIOT), Salem-637504, Tamil Nadu, India.

[c] Department of Sciences & Humanities, Rajiv Gandhi Institute of Petroleum Technology, Jais, Uttar Pradesh, India

[d] Department of Materials Science, Central University of Tamil Nadu, Thiruvarur, Tamil Nadu.

[e] Research Centre for Carbon Solutions, Institute of Mechanical, Process & Energy Engineering, School of Engineering & Physical Sciences, Heriot-Watt University, UK

Abstract

In this work, a clear increase in electrical mobility and absorption coefficient has been demonstrated in spray pyrolysis deposited $CuInS_2$ (CIS) thin films by ruthenium (Ru) doping. This film was then employed as an efficient absorber layer in superstrate photovoltaic cells for the first time. Ru doping into the CIS tetragonal crystal structure increases the tensile strain causing structural modifications including average crystallite size and dislocation density. Further, the Ru causes an adjustment in the Brillouin zone boundary of the CIS semiconductor leading to alternative morphologies on the surface of the substrate such as particles (2 wt.%), rods (4 wt.%), and leaf-like mixed nanoparticles (6 wt.%). The absorbance and emission properties of this CIS absorber layer were studied for possible enhancement in optical properties due to the surface modification. A higher absorption coefficient (1.20×10^6 cm^{-1} compared to pristine CIS 0.84×10^6 cm^{-1}) was observed in the Ru doped CIS film. The possibility for Ru-4*d* to S-3*p* transition explains the electronic origin of an enhanced absorption coefficient in Ru doped CIS thin films. The atomic elements such as Cu, In, S, and Ru and their corresponding 1^+, 3^+, 2^- and 4^+ oxidation states remained unchanged following doping illustrating an intact lattice. The Ru-doped CIS films, optimised at 6 wt.% exhibited both higher electrical and photo responses as compared to a pristine CIS film. Solar cells were fabricated using the

ITO/AZO/CdS/$CuInS_2$ superstrate configuration with and without the Ru doping (0 and 6 wt.% Ru doped CIS)/Au showing an increase from 2.84% to 4.46% PCE a 1.62% increase overall. Following this, similar durability over 500 hours was observed in both device types.

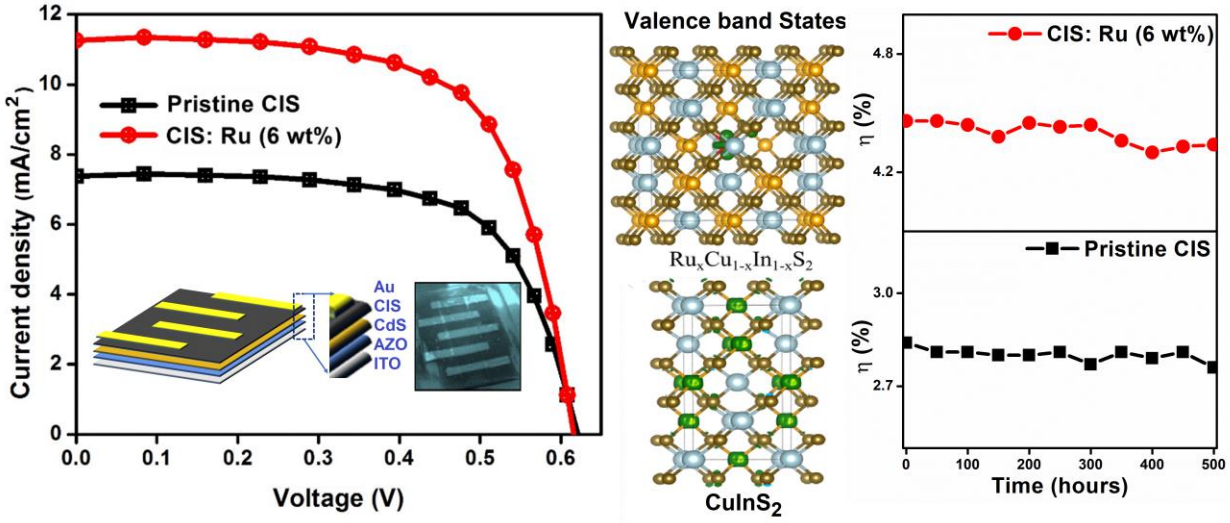

Graphical Abstract

Keywords: $CuInS_2$, Ru-doping, Spray pyrolysis, Absorption coefficient, Solar cell

Corresponding Authors: Logu Thirumalaisamy astrologu10@gmail.com, Sethuraman Kunjithapatham sethuraman_33@yahoo.com

1. Introduction

A rising global population and increase in industrial demand have led to immense power requirements. Unfortunately, consuming more fossil fuels is unsustainable and so alternative energy sources, such as solar, are being explored with a focus on those that contain earth-abundant materials available at a low cost. Over the last decade, polycrystalline $CuInS_2$ (CIS) is a ternary chalcopyrite semiconductor being used as an absorber layer in photovoltaic technology owing to its direct and narrow bandgap traits in the E-k space region [1,2]. The advantage of CIS is its ability to trap more near infra-red energy photons (E= hν) from the solar spectrum [3,4]. Also, CIS fits the I-III-VI group of semiconductors with a tetrahedral phase structure and high absorption coefficient value of approximately 10^5 cm^{-1}. Very specifically, none of its component elements such as Cu, In, and S are toxic [5]. Typically, CIS exhibits in three different crystalline

phases, chalcopyrite, zinc blende, and wurtzite [6], in which the chalcopyrite phase is the most popular due to its high thermal stability. Besides its use in a solar cell, CIS also acts as an effective electrochemical biosensor [7], electroluminescent quantum dot light-emitting device [8], and as photoelectrodes in a photoelectrochemical cell (PEC) [9–11]. In terms of its processability, CIS can be deposited using varying techniques [12–20] including simple methods such as spray coating providing a straightforward route to industrial application.

This work seeks to enhance the absorption coefficient of the CIS material by altering its morphology. Previous work has shown that Al doping of the ZnO layer, which typically acts as an electrode in a CIS solar cell, leads to a honeycomb structure with reduced reflection losses [21] and increased photon harvesting. A similar doping strategy to increase optical absorption is employed in this work. However here it is the CIS layer that is modified. Given that enhancements are observed through changes to the CIS/CdS interface an inversion in the device configuration to a superstrate structure is required [22,23].

A survey of the literature was undertaken to identify a suitable dopant for the CIS absorber layer, that would achieve an optical enhancement. Previously Cd, V, Al, Bi, Zn, Sb, and Yb elements [24–31] have been tested as dopants in the CIS crystal system and have shown a variety of desirable electrical, structural, morphological, and optical properties. However, Ru has not been demonstrated previously as a dopant for CIS despite its central role in other solar technologies such as the dye-sensitized solar cell. Ru was chosen as a doping candidate because of its ionic radii difference when compared to the host ions, the difference suggests the potential for lattice distortion and alteration of the Brillouin zone. Furthermore, from an electrical perspective, Ru doping with respect to its different oxidation states (Ru^{3+}, Ru^{4+}, Ru^{5+}) is likely to increase the carrier concentration and conductivity of the CIS host material without affecting its crystal structure [32,33]. Therefore, a small amount of Ru doping into the CIS lattice would enhance the free electrons resulting in reduced phonon scattering.

A range of doping concentrations was tested from 0 to 8 wt.% and the films were deposited using spray pyrolysis and analysed using electrical and optical techniques. Following optimisation of the doping level (0, 2, 4 and 6%), a superstrate solar cell was constructed using the configuration (ITO/AZO/CdS/CIS absorber layer/Au). Overall, the PCE increased from 2.84% to 4.46% when using Ru doping. This manuscript sets out to understand and explain the

effect of Ru doping on the CIS film and subsequent solar cells. The Ru doping of the CIS structure and subsequent efficiency enhancement is achieved via a simple addition to the precursor chemistry prior to spraying, no additional fabrication processes are required.

2. Experimental details.

2.1 Thin-film preparation

In order to analyse the behaviour of stand-alone CIS films the precursor solution was initially deposited onto plain glass microscope slides by chemical spray pyrolysis technique using copper (I) chloride, indium (III) chloride, and thiourea as source materials for Cu, In and S respectively. For coating, initially, these source materials were dissolved discretely in double distilled (DD) water in the ratio of 1:1:2, and equal volumes of these solutions were mixed and sprayed onto microscope slides of 2.5 × 2.5 cm^2 dimension with a thickness of 0.15 cm. To prevent chemical precipitation, the copper (I) chloride solution was primarily mixed with indium (III) chloride solution and then thiourea solution was added. A surplus quantity of thiourea was also added to the resultant spray solution in order to balance sulphur insufficiency in the deposited film. For Ru doping, ruthenium (III) chloride (2, 4, and 6 wt.%) was chosen and added to the precursor solution. For every single coating, the substrate to nozzle distance was retained at 29 cm. Other important spray factors such as substrate temperature, carrier gas pressure, spray time, and spray rate were also tuned to obtain a good quality Ru doped CIS thin film. The optimized substrate temperature for the entire deposition work was kept at 240 °C and sulphurized at 450 °C.

2.2 Computational methods

For calculations of the atomic and electronic structure of the pristine CIS unit cell and Ru doped 2×2×1 supercell, we have followed the projected augmented wave pseudopotentials traditionalism for describing electron-nucleus interactions within a plane-wave based density functional theory tactic, as executed in the Vienna Ab initio Simulation Package (VASP). The electron-electron interactions were modified with the GGA+U framework methodology; the effective U value for the Cu and Ru metal sites is 6.8 eV and 1.7 eV, respectively. The unit cell volume and all the atoms were fully relaxed with no care about symmetry and the relaxation was iteratively performed till the absolute forces on every ion becomes fewer than 0.01 eV/Å. The

convergence for the wave function optimizations was set to be 10^{-6} eV. For pristine CIS and Ru-substituted CIS, spin-polarized calculations were performed with the aforementioned parameters and methods.

2.3 Device fabrication

Superstrate solar cells with a surface area of 0.126 cm^2 were fabricated with the configuration ITO/AZO/CdS/CIS/Au electrode [34]. The schematic depiction of thin-film deposition and device fabrication is illustrated in Fig.1. For this, initially, ITO coated glass substrates (Sigma-Aldrich surface resistivity 8-12 Ω/sq) were patterned by 1 mil polyimide film tape acrylic adhesive, and then the remaining portion of the substrate was etched by hydrochloric acid. Then the substrates were cleaned with a soap solution and double-distilled water and ultrasonicated for 10 min in acetone and isopropyl alcohol (IPA) separately. Lastly, UV-ozone treatment was carried out to eliminate organic impurities. The bottom Al-doped ZnO (AZO) layer with a thickness of ~700 nm was coated on ITO substrate using the chemical spray pyrolysis technique at 240 °C and annealed at 400 °C. After this, the same technique was used to deposit a ~70 nm thick CdS buffer layer over the AZO layer at 200 °C, and finally, a ~1.5 micron thick pristine and Ru doped CIS absorber layer was coated using the same chemical spray pyrolysis method and then sulphurized with 1 g of sulphur powder using a tubular furnace in the nitrogen atmosphere at 450 °C for 20 min. For the back contact, a ~200 nm thin Au layer was prepared on top of the CIS by thermal evaporation at room temperature. Here, the deposition chamber pressure was maintained at 4×10^{-6} mbar and evaporated at a rate of 8−11 Å/s for 2 min 30 sec.

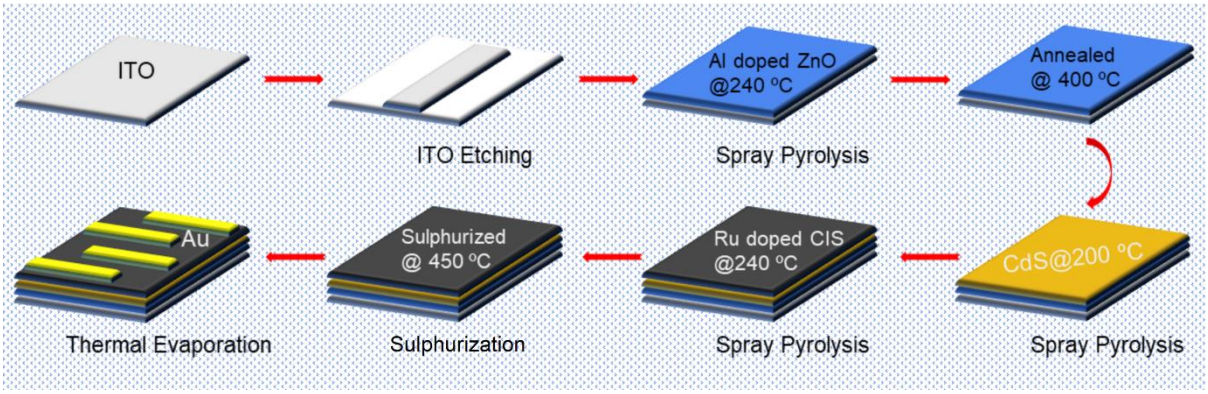

Fig. 1 *Schematic depiction of thin-film deposition and device fabrication.*

2.4 Characterization

For characterization of the active layer (pristine and Ru doped) a Perkin Elmer Lambda 950 spectrometer was used for studying the optical absorption properties and a SHIMADZU-5301 spectrofluorometer was used for examining the optical emission properties. The impact of Ru in the host spatial lattice induces the crystallographic behaviour changes, which were then probed using X-ray diffraction (Brucker D8 Advanced X-ray diffractometer instrument). The surface morphologies were then characterized using Field Emission Scanning Electron Microscopy (FESEM) (Model: Nova Nano SEM 230). The crystal structure and morphologies were further confirmed using High-Resolution Transmission Electron Microscopy (HRTEM) JEOL (Model: JEM 2100). Shimadzu ESCA – 3400 X-ray Photoelectron Spectroscopy (XPS) was used to determine the presence of elements (host (CIS) and guest (Ru)) and their oxidation states. A Ambios, XP2 surface profiler was employed to determine the thickness of the prepared thin films, and then the electrical parameters were analysed using Hall measurement (Ecopia HMS-3000). A Holmarc contact angle analyser was used for testing wettability characteristics. To measure photocurrent, a Tektronix, Model: 6487 HHV cryostat instrument was used at ambient temperature. The photovoltaic cell parameters such as open-circuit voltage, fill factor, short-circuit current, and conversion efficiency were measured on pristine and 6 wt.% Ru doped CIS films using a AAA solar simulator under standard AM 1.5 G conditions.

3. Results and discussions

Typically, CIS is an absorber layer and so the quantity of light absorbance and the absorption edge point are the most significant factors for determining whether deposited samples will be an effective absorber material or not. Therefore, absorption spectra have been taken for the prepared thin films in the wavelength range of 390 to 1200 nm, and the spectra are displayed in Fig. 2(a). It is evident that all Ru doped CIS films show higher absorbance as compared to pristine CIS film in which 6 wt.% Ru doped CIS film shows the highest value. The absorption coefficient value is a matter for good light harvesting phenomenon and hence the same for 0, 2, 4, and 6 wt.% Ru doped CIS films were estimated, which were 0.84×10^6 cm^{-1}, 1.08×10^6 cm^{-1}, 1.10×10^6 cm^{-1}, and 1.20×10^6 cm^{-1} in the 390-850 nm region of solar spectrum. These values are suitable for covering high-energy distributed sunlight photons [24].

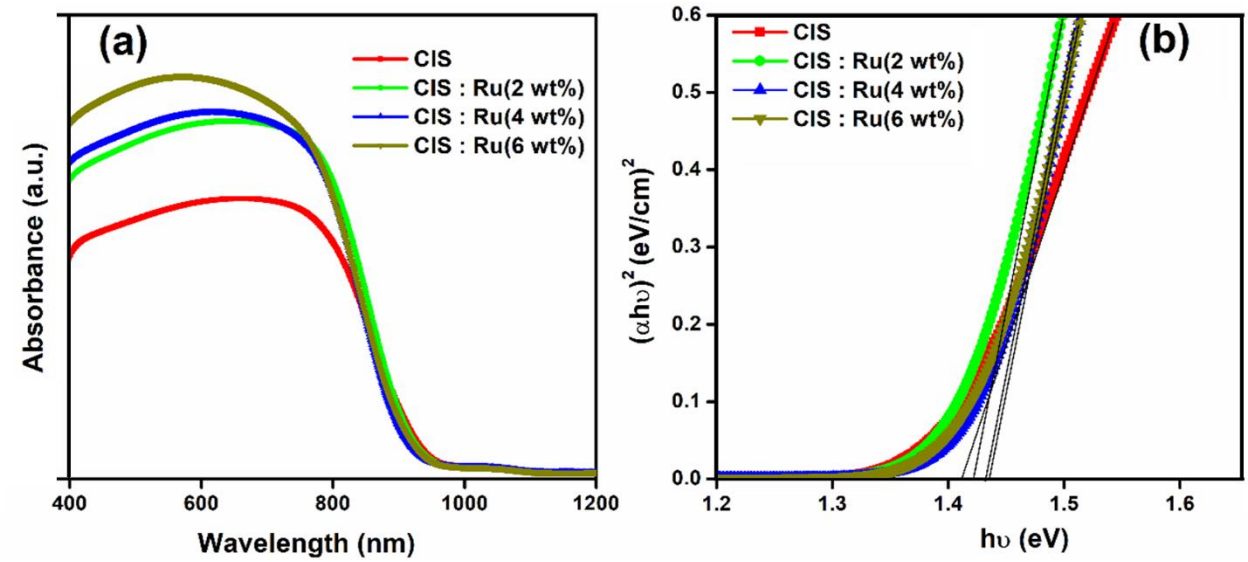

Fig. 2 *(a) Absorption spectra, (b) Optical band gap of pristine and Ru-doped CIS films*

The Tauc plot (Fig. 2(b)) has been drawn between photon energy and absorption coefficient for determining energy band gap values of Ru doped (0, 2, 4, and 6 wt.%) CIS films. The optical band gap (Eg) of the corresponding films are 1.431, 1.433,1.432, and 1.433 eV. As expected, increasing Eg value with small magnitude in the prepared Ru doped CIS films is due to changing of atoms from their relative lattice sites.

Fig. S1 demonstrates the photoluminescence (PL) emission spectra of Ru doped (0, 2, 4, and 6 wt.%) CIS films. Here, the PL emissions at 881 nm for all the prepared films indicate that luminescence occurs by radiative decay of excitons from the semiconductor CIS system[25]. The short PL peak intensity with Ru doping in the CIS lattice and the low exciton rate confirms that the quenching effect is more distinct in the higher Ru doping level. The PL data suggests that Ru doped CIS films aid charge carrier extraction and show promise as an enhanced absorber layer in photovoltaic cells.

To understand how the Ru doping changes the electronic structure of CIS, we first studied the bulk CIS within the GGA+U framework as detailed in the computational methods section [35]. Then, a 2×2×1 supercell was considered as the ***c*** lattice parameter (11.251 Å) of pristine CIS, and this was significantly larger than the ***a*** and ***b*** parameters (5.594 Å, 5.594 Å). The pristine CIS unit-cell shows a direct bandgap of 0.6 eV (Fig. 3) within the GGA+U formalism in which the valence band states are arising mainly from the Cu-3*d* orbitals whereas

the conduction band states are mainly arising from the S-3*p* orbitals as plotted in Fig. 4. During the photoexcitation, the electrons are promoted from the Cu-*3d* to S-3*p* orbitals in the pristine CIS. Further to study the effect of Ru doping, a Ru atom is substituted at the In site in the supercell (6.25% Ru doped CIS) to evade the interaction between the Ru and its periodic image. When the Ru is in the tetrahedral field of S atoms, the *d* orbitals split into e_g and t_{2g} groups. The doubly degenerated e_g states are lower in energy than the triply degenerated t_{2g} states. Since the Ru is substituted in the In^{3+} site, Ru takes a 3+ oxidation state with 5 *d*-electrons, out of which four electrons fill the e_g states and the remaining one electron fills a t_{2g} level.

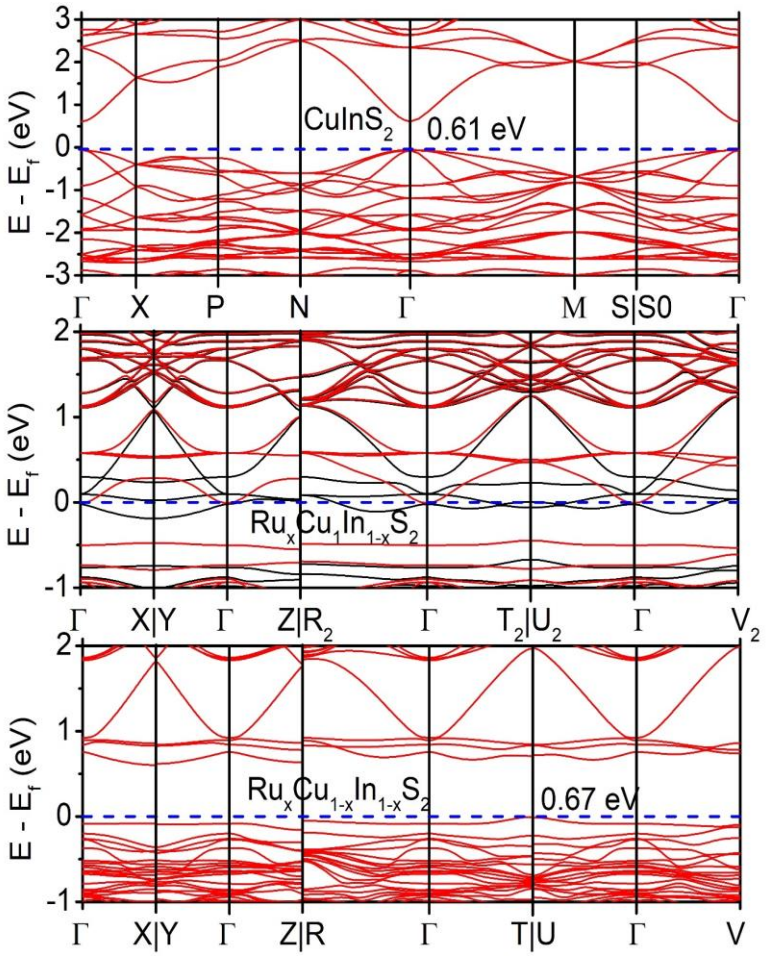

Fig. 3 *Electronic band structure of $CuInS_2$ (Top), $Ru_XCu_1In_{1-x}S_2$(without Cu-vac), and $Ru_xCu_{1-x}In_{1-x}S_2$(with Cu-vac). The energy scale is calibrated with respect to the Fermi energy of the systems.*

From the band structure (Fig.3), it is clear that the Fermi level is lifted near the conduction band due to the filling of a t_{2g} state. However, from the experiment, it is understood that the pristine CIS samples are p-type in nature due to the presence of Cu vacancies [36]. Thus, we have extended our studies to check the electronic structure of Ru doped CIS in the presence of a Cu vacancy which can scavenge the electrons filled in the t_{2g} of Ru^{3+}.

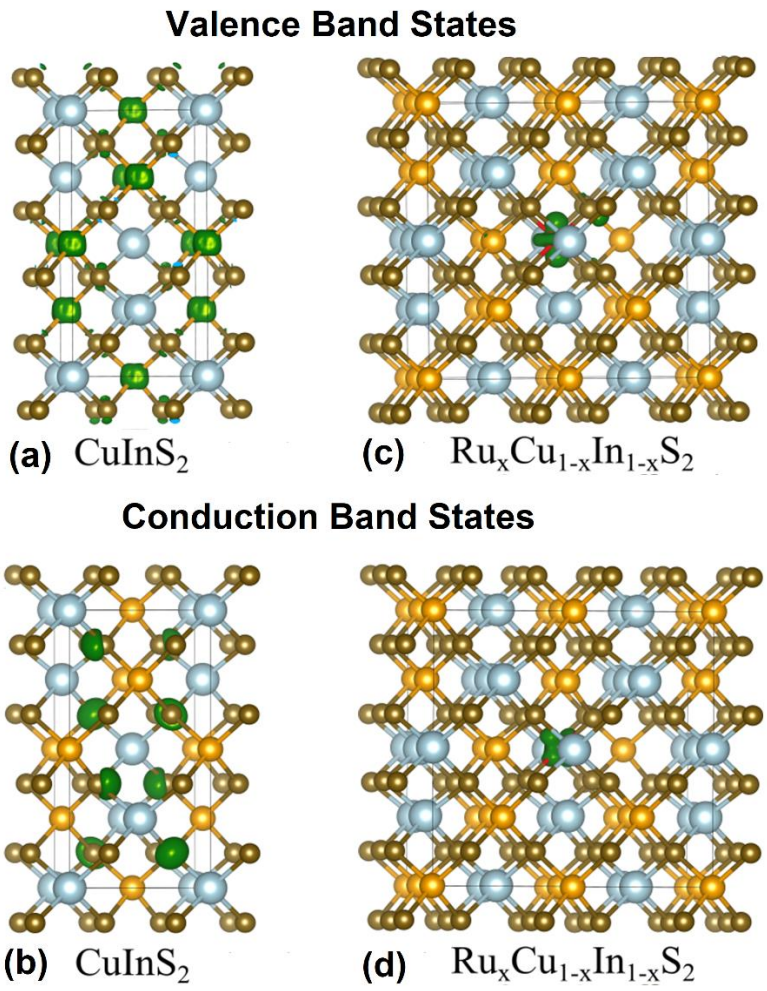

Fig. 4: *(a, c) Valence Band (VB) and (b, d) Conduction Band (CB) states of $CuInS_2$ and $Ru_xCu_{1-x}In_{1-x}S_2$. The orange, silvery-grey, brown, and red colour balls represent Cu, In, S, and Ru atoms, respectively. The green colour isosurface shows the valence and conduction band states. In (a), the Cu atoms are covered inside the isosurface of VB states and in (c and d) the Ru atoms are covered with isosurface.*

Thus, in a system with a Cu-vacancy, the Ru^{3+} can be oxidized to Ru^{4+} with a clear opening of bandgap encompassing the t_{2g} and e_g states in between the VB and CB of pristine CIS. Hence, a Cu atom is removed in the Ru doped system to obtain its atomic and electronic structure. As expected, the calculated band structure shows a clear opening of the bandgap because the Ru atom goes to the +4 oxidation state donating one electron to fill the unsaturated state of S atoms around the Cu vacancy. In addition, the filled e_g states and empty t_{2g} states are encompassed between the valence and conduction band of CIS. These states increase the density of states near the valence and conduction band edges (Fig. 3). In the presence of Ru^{4+} substituted at the In^{3+} site with a Cu^{1+} vacancy, the least dispersed e_g and t_{2g} states of Ru-4*d* orbitals lie above the VB and below the CB of pristine CIS bands. However, the electronic bandgap does not change much after Ru doping in the CIS with Cu vacancy. Due to the presence of Ru-4*d* states near the VB and CB of CIS, a strong *d-d* transition is also possible as Ru is lacking a center of symmetry in the tetrahedral coordination. In addition, there is a possibility for Ru-4*d* to S-3*p* transition. This clearly explains the electronic origin of an enhanced absorption coefficient in Ru doped CIS films.

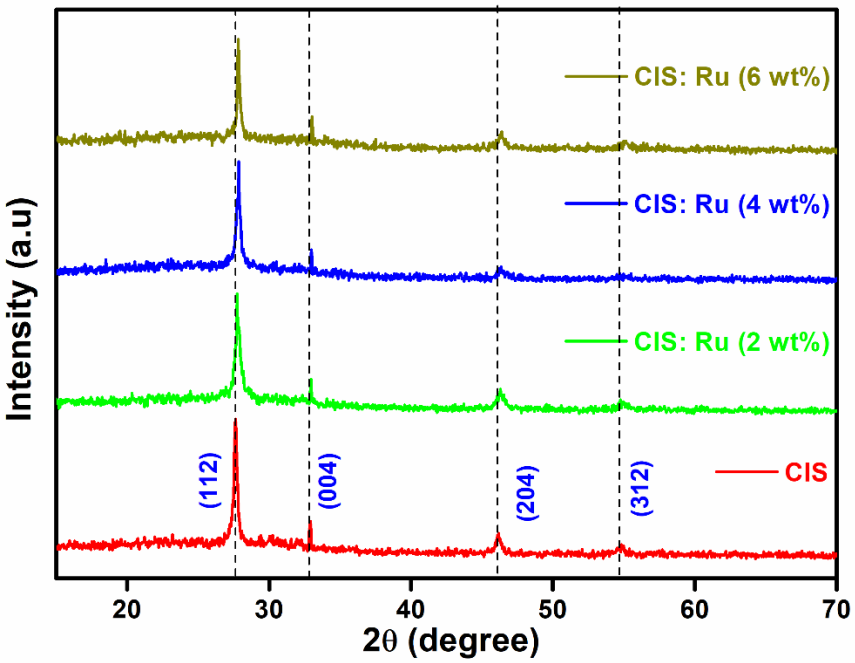

Fig. 5 *XRD pattern of pristine and Ru-doped CIS films*

To find out which structural imaginary lattice sites are permitted to localise basis (Cu, In, S) and how many crystalline planes (crystallinity) are involved in building a real crystal

structure, XRD is commonly used in which the wave vector (k-space) of the material is used for detecting diffraction patterns. XRD patterns of deposited films including 0, 2, 4, and 6 wt.% Ru doped CIS are shown in Fig. 5. All detected patterns are well-matched with the standard data JCPDS NO. 32-0339 and confirm the formation of the tetragonal chalcopyrite phase. In the case of the pristine CIS film, the (112) crystal plane is a dominant one. The intensity of this plane decreases with increasing Ru doping levels. This result is likely due to the increasing disturbance of lattice spaces of the (112) crystal plane growth by dopant during deposition [30]. As expected, the diffraction XRD peaks are slightly moved to a higher 2θ angle with a rising Ru dopant level as compared to the undoped CIS film. The slight peak shift is typically due to the inclusion of Ru dopant in the CIS crystal lattice [25]. The calculated lattice constants in 6 wt.% Ru doped CIS are 54.98 nm for a and 108.89 nm for c which were found to be slightly less than the un-doped CIS film where a = 55.17 nm and c= 110.06 nm [24]. The reason for this result is the ionic radius of the Ru^{4+} ion is less than the ionic radius of Cu^{+} and In^{3+} ions. No secondary characteristic XRD peaks of additional impurities were observed such as RuS_2, In_2S, or Cu_2S. The size of the crystallite and dislocation density are also calculated using the well-known Scherer and Williamson and Smallman's formula respectively [37]. As expected, increased crystallite size and decreased dislocation density are attained for Ru doped CIS films. The observed values are displayed in Table. 1

Table 1. *The structural parameters and bandgap of pristine CIS and Ru-doped CIS films*

Sample	Average crystallite size (nm)	Average dislocation density ($x10^{15}$ lines/m^2)	Band Gap (eV)
CIS: Ru (0 wt.%)	20	3.28	1.431
CIS: Ru (2 wt.%)	22	2.46	1.433
CIS: Ru (4 wt.%)	25	2.27	1.432
CIS: Ru (6 wt.%)	29	2.01	1.433

With the aim of confirming the presence of Ru in the lattice of CIS, the 6 wt.% Ru-doped CIS thin-film was subjected to XPS analysis. In CIS film, peaks at 951.3 and 931.9 eV are related to the binding energies (BE) of $Cu2p_{1/2}$ and $Cu2p_{3/2}$ states (Fig. 6(a)) and strongly confirm the +1 oxidation state of Cu ions. Further, the binding energy peaks at 445.7 and 451.5 eV are owing to $In3d_{3/2}$ and $In3d_{5/2}$ orbitals (Fig. 6(b)) indicating that In is in a +3 oxidation

state. Further, a peak at 167 eV confirms the S2p state (Fig. 6(c)). For the Ru doped film, an additional peak at 281.4 eV (Fig. 6(d)) infers the presence of $Ru3d_{5/2}$ orbitals and suggests that Ru interacts with the CIS lattice in an +4 oxidation state. Neither other additional peaks nor derivative phases confirm the single S environment or the presence of RuO_2, Ru_2S_3, and Cu_2S secondary phases.

The elemental compositions of Ru doped (0, 2, 4, and 6 wt%.) CIS thin films were checked additionally by EDAX analysis, and their elemental compositions values are provided in table 2. The observed Ru dopant quantity in the deposited film is 1.86 %, 3.56%, and 5.54% for 2, 4, and 6 wt.% Ru doped CIS films confirming the accuracy of the precursor preparation. From table. 2, it is noticed that 1.22% variation in Cu ions and 4.67% variation in In ions are reduced with increasing Ru dopant level up to 6 wt.%. The 1% of Cu ion variation generally occurs even when dopants are not introduced because of the higher mobility of Cu ions in their lattice space [38]. This result specifies that doping of Ru mostly finds a place in the lattice space of In sites in the CIS crystal system.

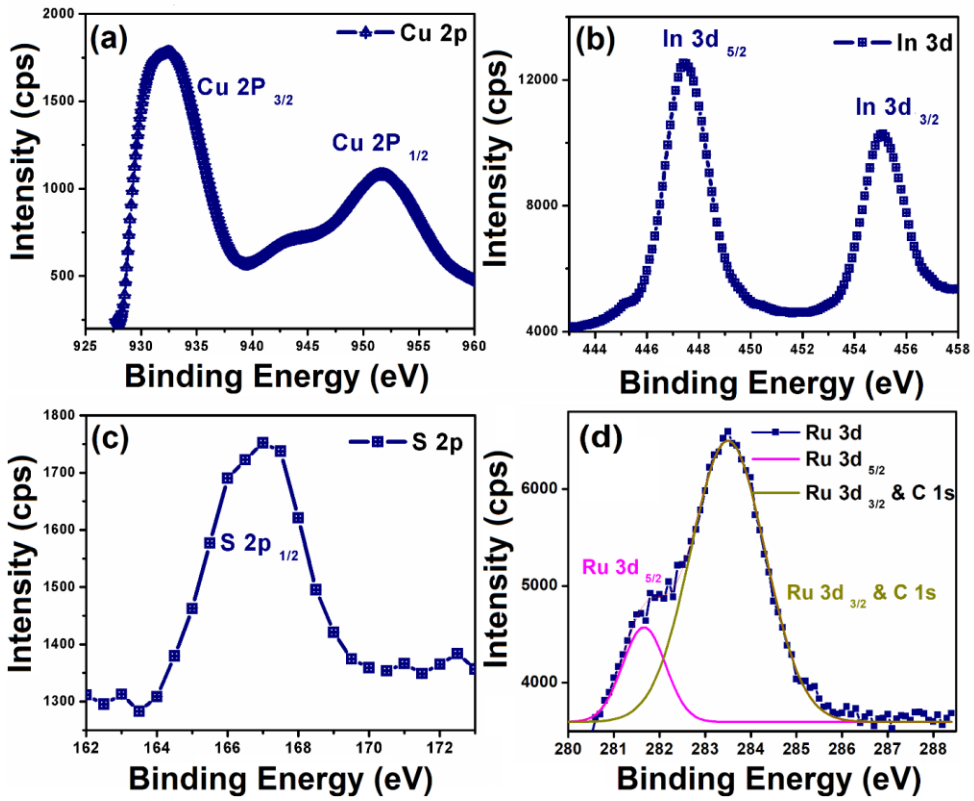

Fig. 6 *XPS spectra of CIS: Ru (6 wt%) film: (a) Cu:2p, (b) In:3d, (c) S:2p, and (d) Ru:3d*

Table 2 *The elemental composition of pristine and Ru doped CIS films.*

Sample	Cu (wt%)	In (wt%)	S (wt%)	Ru (wt%)
CIS: Ru (0 wt.%)	24.18	25.86	49.96	0.00
CIS: Ru (2 wt.%)	24.13	23.45	49.86	1.86
CIS: Ru (4 wt.%)	24.53	21.98	49.93	3.56
CIS: Ru (6 wt.%)	23.96	20.24	50.26	5.54

Fig. 7 illustrates FESEM images of pristine and Ru doped CIS films. The pristine CIS thin film on the glass substrate seems to be uniform with spherical-shaped nanoparticles (Fig. 7(a)). Firstly, an overview of Ru doped CIS samples confirms that surface morphology considerably changes after the doping of Ru (Fig. 7(b-d)). Due to the changes in growth mechanism (heterogeneous, homogeneous, and mixed of both), the fine spherical nanoparticle film changes after doping. Therefore, the 2 wt.% Ru doped CIS film displays an uneven surface composed of micro-sprout-shaped particles.

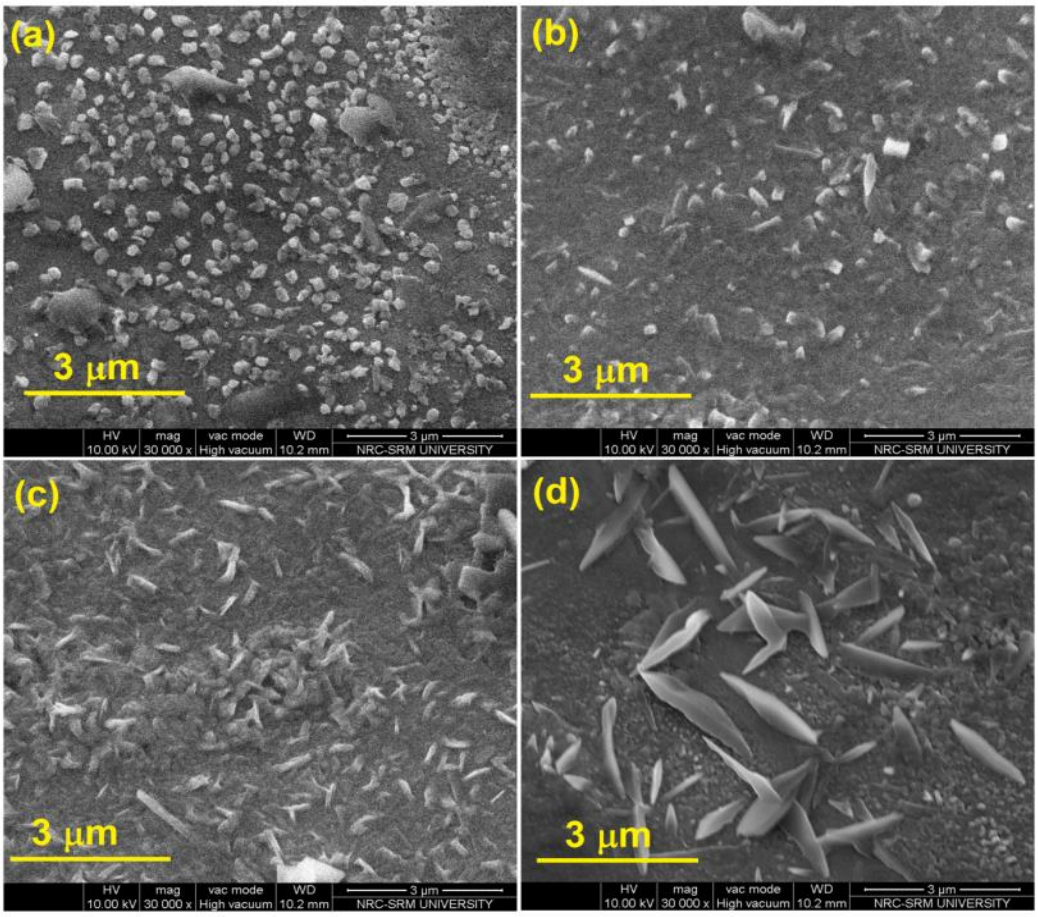

Fig. 7 *FESEM images of (a) pristine CIS, (b) 2 wt.%, (c) 4 wt.%, and (d) 6 wt.% of Ru-doped CIS.*

A randomly oriented micro-rods structure is observed with 4 wt.% Ru-doped CIS film. We know that there are three growth mechanisms such as heterogeneous, homogeneous, and mixed of both are played a chief role in deciding the surface morphology of spray deposited film. Here, the obtained morphology undoubtedly says that the mixed mechanism (homogeneous as well as heterogeneous) is engaged throughout the aerosol decomposition over the surface of the substrate concerning growth time and doping level [24]. Further, the nanorods and micro leaf structured morphologies are found to be homogeneously distributed in the 6 wt.% Ru-doped CIS film. These changing morphologies imply that the introduction of the Ru dopant with the various concentrations in the CIS lattice strongly affects the growth evolution of CIS nanostructures. The dopant ions are easily intermingling with the host ions and form aggregation before depositing on the substrate and fulfilling the foremost homogeneous mechanism. Therefore, it reveals that

Ru doping in CIS film changes the spray growth mechanism, resulting in spherical particles to micro leaves morphologies.

Transmission Electron Microscopy (TEM) images, Selected Area Electron Diffractions (SAED) pattern, and High-Resolution Transmission Electron Microscope (HRTEM) d-spacing images of the Ru doped (0, 2, 4, and 6 wt. %) CIS thin-films are depicted in fig. 8 (a1–c1), (a2–c2), (a3-c3), and (a4-c4). CIS thin-film is comprised of tiny spherical-shaped particles with a size of ~ 40 nm (Fig.8a1). The prepared CIS film's SAED pattern is presented in fig. 8(b1) and illustrates diffused rings as CIS film of a polycrystalline nature. The concentric circles indexed corresponds to the tetragonal phase. The CIS lattice fringes show ~0.315 nm interplanar spacing and this is attributed to the tetragonal crystal structure (112) crystallographic plane. The TEM image of the 2 wt.% Ru doped CIS film (Fig. 8(a2)) reveals the cluster of agglomerated nanoparticles aggregated to micro rods. The interplanar lattice spacing of ~0.312 nm is noted, which is analogous to the (112) crystallographic plane and is matched with previously reported HRTEM images [26]. Fig. 8(a3) shows a TEM image of the 4 wt.% Ru doped CIS film which shows micro-rod morphology. The interplanar lattice spacing of ~0.307 nm is correlated through the (112) plane. Fig. 8 (a4) shows the TEM image of 6 wt.% Ru doped CIS film that undoubtedly exposes micro leaf structured particles. The SAED patterns (fig. 8b1 to b4) confirm that all the films deposited have a polycrystalline nature of tetragonal crystal structure. This outcome firmly validates the XRD results as well. The CIS lattice fringes value decreases up to 0.012 nm with Ru doping and indicates that tensile strain is formed by adjusting the Brillouin zone boundaries.

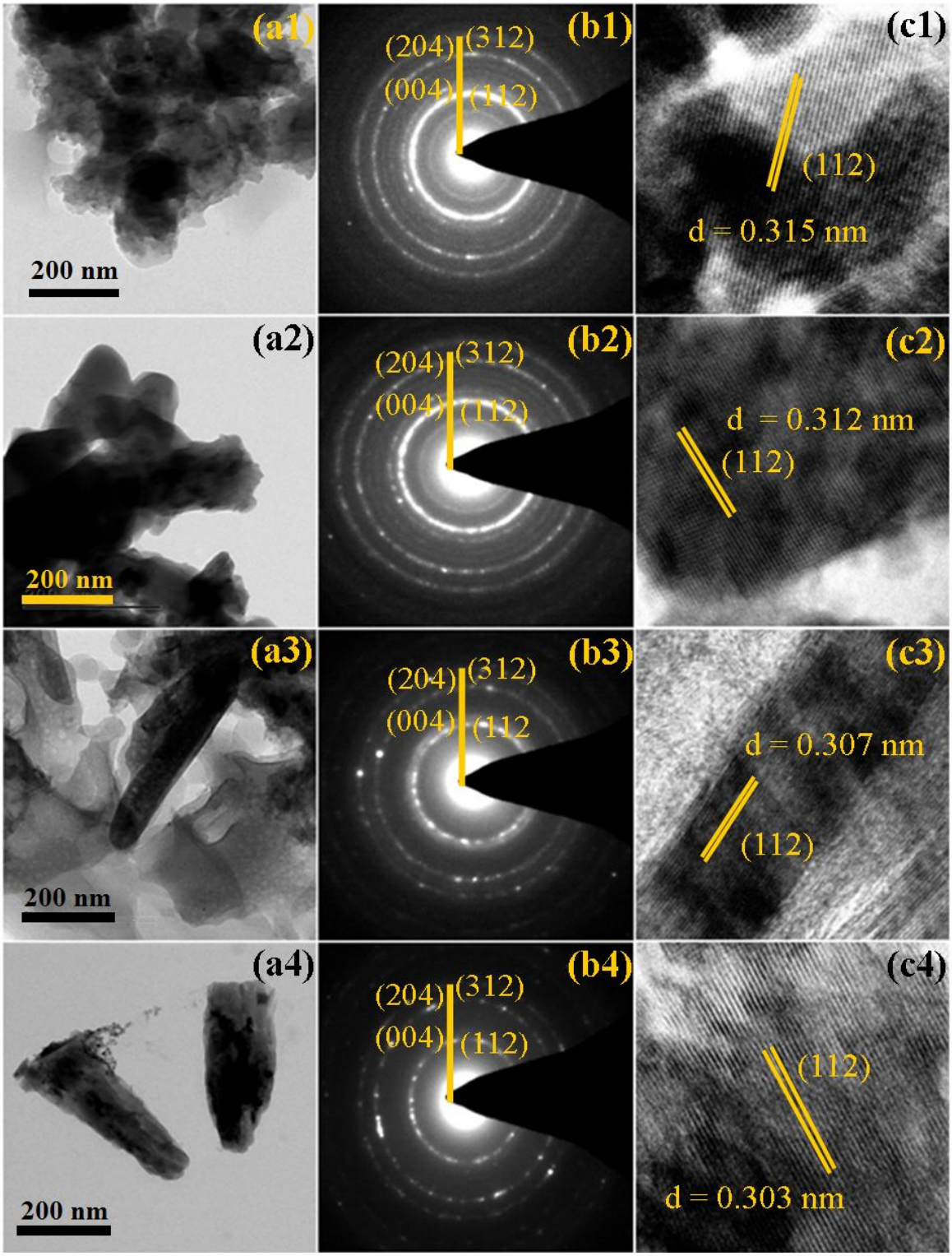

Fig. 8 *(a1–c1), (a2–c2), (a3-c3), and (a4-c4) illustrate the TEM image, SAED pattern, and HRTEM d-spacing of pristine, CIS: Ru (2, 4 and 6 wt%) film.*

Table. 3. *Electrical parameters of pristine and Ru doped CIS films*

Sample	Resistivity (ohm-cm)	Carrier Concentration ($\times 10^{18}$ cm^{-3})	Mobility (cm^2 $V^{-1}s^{-1}$)	Conduction Type
CIS: Ru (0 wt.%)	1.189	1.88	3.61	*p*
CIS: Ru (2 wt.%)	0.0461	3.89	34.79	*p*
CIS: Ru (4 wt.%)	0.00159	41.8	82.91	*p*
CIS: Ru (6 wt.%)	0.00151	44.9	96.89	*p*

The electrical parameters (resistivity, Hall mobility, and carrier concentration) of 0, 2, 4, and 6 wt.% Ru-doped CIS films were measured at ambient temperature using four-probe Hall measurements. Fig. S2 provides electrical parameters (carrier concentration, resistivity, and Hall mobility) of CIS with Ru doping level respectively, and their magnitude values are given in Table. 3. The positive Hall coefficient of the prepared films endorses the p-type conducting nature [39]. Pristine CIS film possesses high resistivity (1.189 Ω cm), mobility (3.61 cm^2/Vs), and carrier concentration value of 1.88× 10^{18} cm^{-3}. After Ru doping in the CIS lattice, a deterioration in resistivity value was observed. This could be ascribed to a huge number of charge carriers (44.9 × 10^{18} cm^{-3})at Ru the doped CIS films [40]. The majority charge carrier's mobility increases in 2, 4, and 6 wt.% Ru doped films [41]. This indicates a decrease in impurity scattering with Ru doping level [42,43]. Further, when increasing the doping concentration to 8 wt.%, the host $CuInS_2$ film's crystalline quality and electrical properties deteriorated with the influence of impurity ions. The increase of Hall mobility can be ascribed to the enhancement of crystalline quality and crystallite size, which is schematically shown in Fig. S3 (guide to the eye illustration of carrier movement across the grains). The bigger crystallite size results in a lower density of grain boundaries. Therefore, enhancement in the crystallite size reduces grain boundary scattering and increases carrier mobility. On the other hand, as shown in Fig. S3, the reduced mobility (0.78 cm^2/Vs) for films containing 8 wt.% Ru can be ascribed to degraded crystalline quality and smaller crystallite size. Hence, this result confirms that 6wt% Ru is the right dopant for high mobility in p-type CIS absorber material.

In this work, different CIS film morphologies are observed with different Ru dopant levels. To understand the influence of this change in morphology on the surface of the CIS film, a wettability analysis was undertaken [26]. The morphologies that are likely to show the greatest difference in surface behaviour (0% and 6% Ru doping) were chosen for analysis. The spherical-shaped 0% doped CIS film revealed a Contact Angle (CA) of 87° (Fig. S4 (a, c)); whereas 6 wt.% Ru doped CIS film shows the highest CA value, 132° as seen in Fig. S4 (b, d). The spherically shaped surface morphology of CIS film (Fig. S4 (c)) possesses a lower CA value due to increased interaction with the water molecule. In the micro leaf structure (6 wt.% Ru doped CIS (Fig. S3 (d))), trapped air molecules in between each leaf lead to a higher CA value. Hence, this outcome infers that CIS film becomes more hydrophobic with Ru doping.

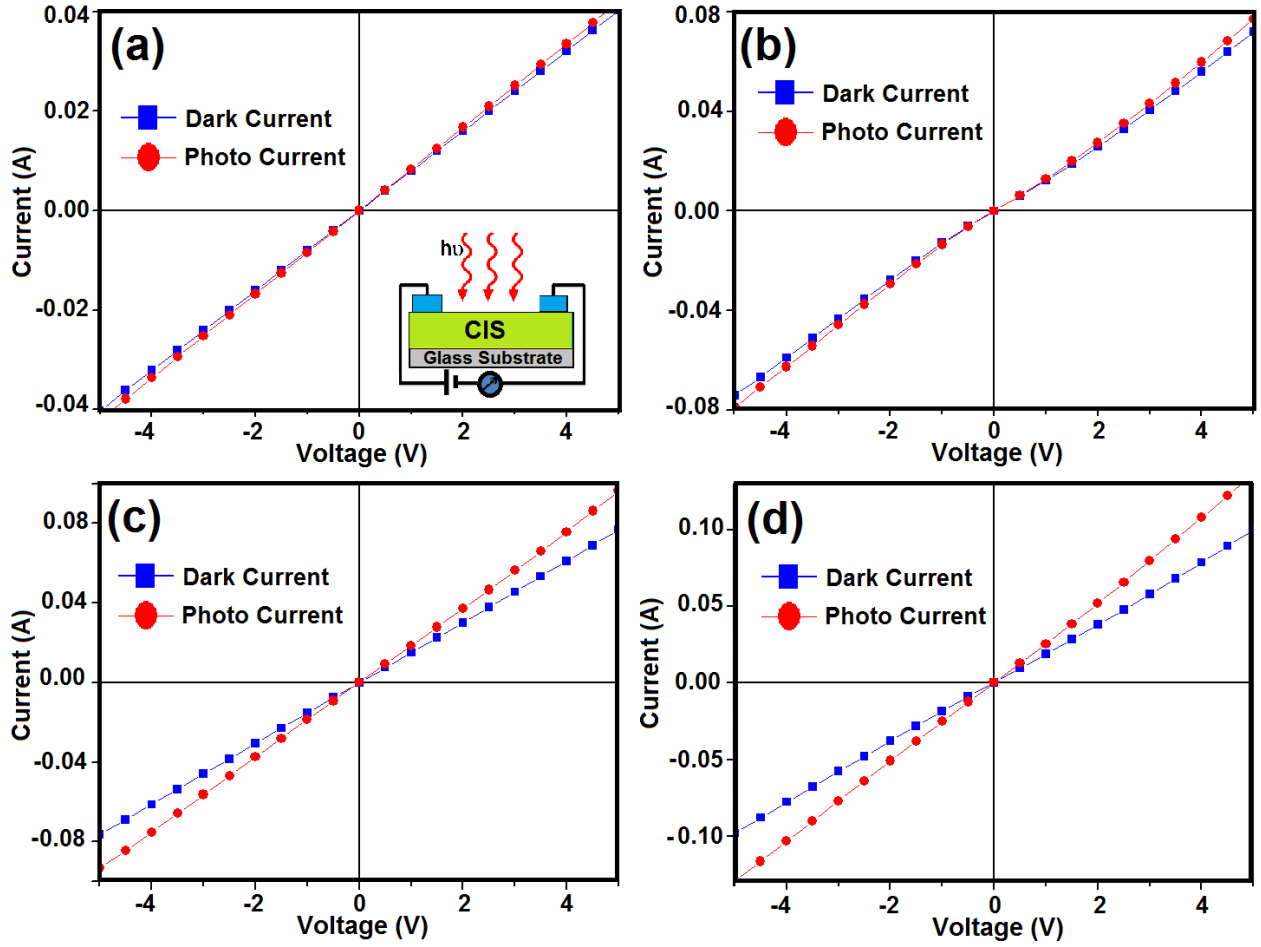

Fig. 9*(a) (inset) Graphic of the photoresponse measurement system. I-V curve in dark and light conditions. (a) pristine, (b) 2 wt.% Ru, (c) 4 wt.% Ru, and (d) 6 wt.% Ru doped CIS film.*

The photo-responses for Ru doped (0, 2, 4, and 6 wt.%) CIS films under dark and light illumination conditions were measured and are displayed in Fig. 9. For this measurement, the electrical contacts were prepared onto the sample at 0.5 cm spacing utilizing thermally evaporated Au and then connected with an ammeter and DC power source in series [44] (Inset Fig. 9(a)). Later, the undoped and Ru doped CIS thin films were illuminated with a 50W xenon lamp and consequent photoresponse was measured with the electrometer [45]. The Ru doped CIS films show higher photoresponse compared to the pristine CIS thin film (Fig. 9(c & d)). This may be due to the stimulation of more photoelectrons under the illumination condition. Generally, the superior absorbance (high absorption coefficient) and good electrical parameters such as mobility, resistivity, and carrier concentration of the films will be the reason for high photo-response [19,23,26,45,46]. In our case, superior photoresponse was noticed in 6 wt.% Ru doped CIS thin film (Fig. 9(d)) and is well-consistent with other dopants demonstrated previously [26,31,47]. The micro sprout and leaf structured Ru doped CIS thin-film absorber could be a better candidate than pristine CIS for producing superior photocurrent in photovoltaic devices.

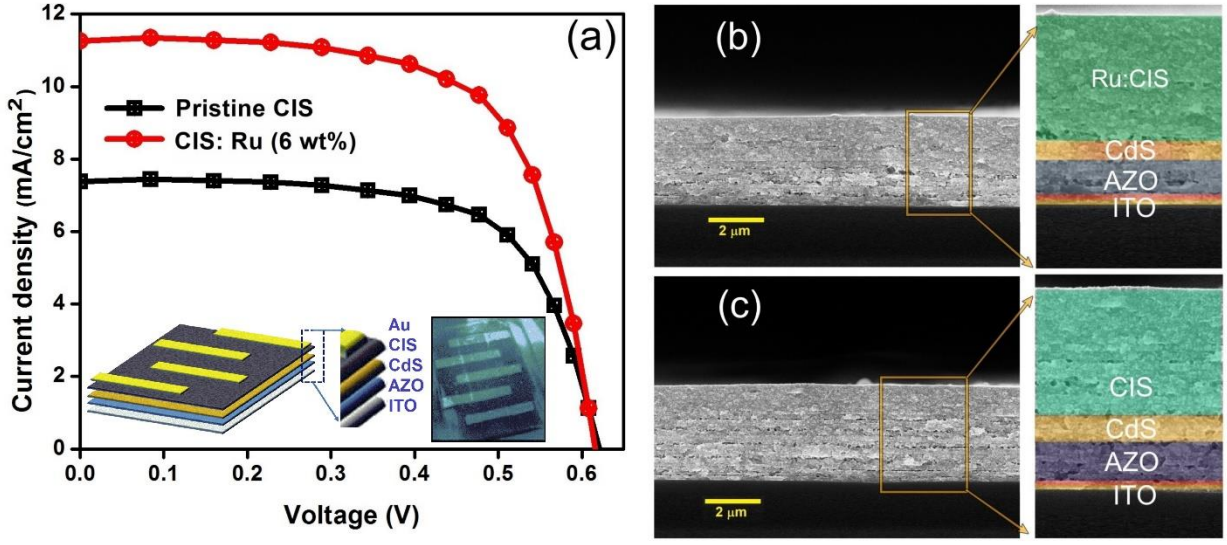

Fig. 10 *(a) J-V characteristics of pristine and 6 wt% Ru doped absorber layer utilized $CuInS_2$ solar cells, cross-sectional SEM image of (b) Ru doped and (c) pristine CIS solar cells.*

The 0 and 6 wt.% Ru doped films are the films where the minimum and maximum absorption coefficient value is observed. Therefore, superstrate device fabrication was undertaken with 0 and 6 wt.% Ru doped CIS film absorber layers. The schematic diagram of the CIS absorber layer-based superstrate solar cell configuration, ITO/AZO/CdS/CIS/Au is given in the inset of Fig. 10 (a) and its corresponding cross-sectional SEM is given in Fig. 10 (b) and (c). The pristine CIS solar cell (ITO/AZO/CdS/CIS/Au) delivered a short-circuit current density (J_{sc}) of 7.39 mA/cm^2, the open-circuit voltage of (V_{oc}) 0.61 V, and fill factor (FF) 0.63 resulting in 2.84±0.07 % efficiency (η). The current photovoltaic performances of the CIS-based superstrate solar cells are summarized in table 4. The 6 wt.% Ru doped CIS solar cell shows higher J_{sc} (11.25 mA cm^{-2}) with an efficiency of 4.46±0.04 % and is greater than other cells tested previously [47-56].

Table 4. *Recent photovoltaic performances of the CIS-based superstrate solar cells.*

Solar cell Structure	**J_{SC} (mA/cm^2)**	**V_{OC} V**	**FF**	**Efficiency %**	**Reference**
ITO/AZO/CdS/CIS/Au	7.39	0.610	63.0	2.84	This work
ITO/AZO/CdS/6wt% Ru:CIS/Au	11.25	0.610	65.0	4.46	This work
ITO/ZnO/In_2S_3/CIS/carbon	12.20	0.430	58.0	3.00	[48]
FTO/TiO_2/In_2S_3/ CIS/Mo	11.20	0.370	35.0	1.70	[49]
FTO/TiO_2/In_2S_3/CIS/Carbon	10.90	0.519	46.0	2.66	[50]
Glass/FTO/CdS/CIS /Au	6.80	0.200	25.0	0.36	[51]
FTO/TiO_2/In_2S_3/CIS/carbon	11.20	0.401	47.3	2.11	[52]
FTO/TiO_2/CdS/ CIS /Au	9.61	0.640	51.4	3.15	[53]
ITO/ZnO NR/NCLD CdS/CIS/Au	10.10	0.669	49.4	3.30	[54]
FTO/TiO_2/In_2S_3/CIS/Carbon	13.80	0.400	38.0	2.07	[55]
FTO/SP-ZnO/NP Cl:ZnO/ In_2S_3/CIS /graphite	13.30	0.500	43.0	2.80	[56]
FTO/ TiO2/ CdS/ CIS/Au	4.30	0.59	46.0	1.20	[57]

This analysis strongly confirms the higher J_{sc} value is due to the high absorption coefficient and high carrier concentration in the leaf-like morphology of 6 wt.% Ru doped CIS absorber layer leads to increased photon harvesting [58]. Therefore, the improved photocurrent drives its

transport leading to enhanced J_{sc} and efficiency. The J_{sc} value enhancement could be the result of the changing of morphologies (aggregated spherical particles to leaf and nanorods mixed structure) that are provoked by tensile strain formation during deposition. In FF value also, 6 wt.% Ru doped absorber layer solar cell exhibits higher FF than pristine CIS cell, this is due to the harvesting of more photons in 6 wt.% Ru doped CIS absorber layer photovoltaic cell. Such a transformation in the morphology of CIS by Ru doping significantly improved the electrical and optical properties leading to increased photovoltaic performance. A long-term stability test was also conducted under AM 1.5 G standard conditions at 25 °C (Fig. 11). Both doped and pristine CIS devices showed good and constant stability even up to 500 hours.

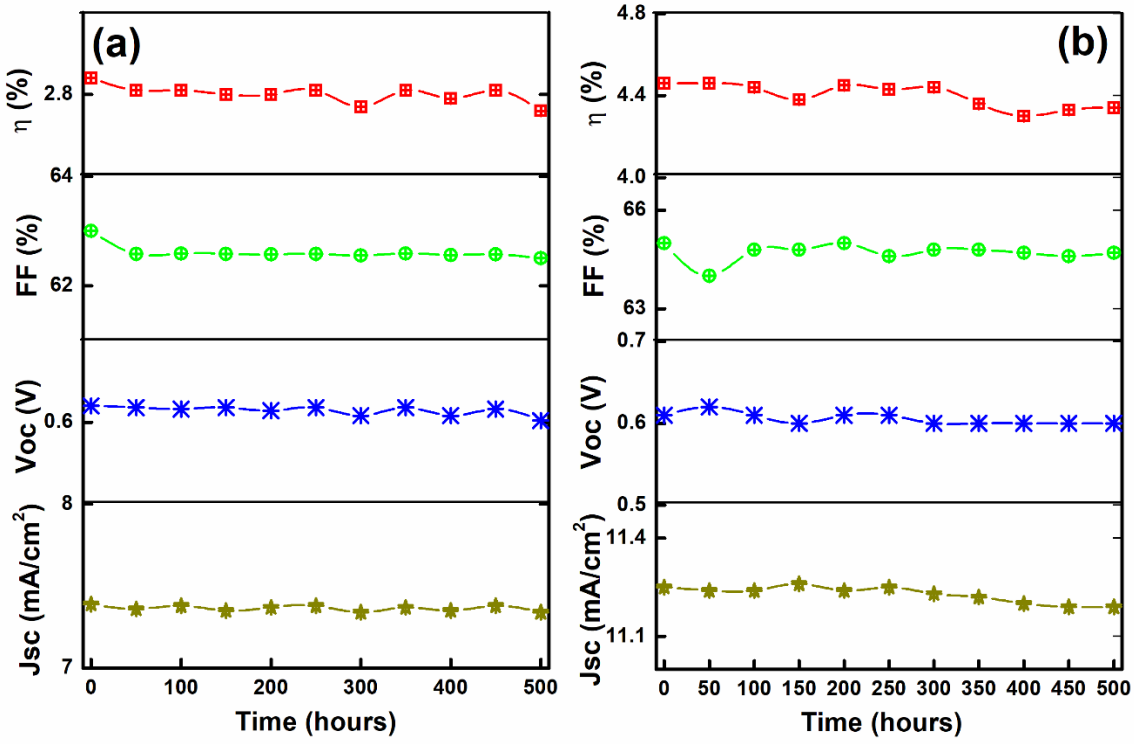

Fig. 11. *Evolution of short circuit photocurrent (Jsc), open-circuit photovoltage (Voc), fill factor, (FF), efficiency (η) of pure and 6 wt% Ru doped CIS solar cell during prolonged room-temperature aging in the dark.*

4. Conclusion

Polycrystalline Ru doped (0, 2, 4, and 6 wt.%) CIS thin films were successfully prepared for the first time using the chemical spray pyrolysis deposition technique. The observed diffraction peaks for all prepared films were indexed and well-matched with the standard

tetragonal crystal structure. All the Ru doped CIS films have a higher absorption coefficient value than the pristine film. It was found that 4 and 6 wt.% Ru doping into CIS modified the surface morphology producing microrod and leaf-shaped microstructures. Ru doping showed higher electron mobility through Hall measurements. Due to the presence of Ru-4*d* states near the VB and CB of CIS, a strong *d*-*d* transition is also possible as Ru is lacking a center of symmetry in the tetrahedral coordination and there is a possibility for Ru-4*d* to S-3*p* transition. This clearly explains the electronic origin of an enhanced absorption coefficient in Ru doped CIS thin films. Therefore, eventually, the best superstrate solar cell device performance using a 6 wt.% Ru doped CIS absorber layer produced a photocurrent density of 11.25 mA/cm^2, the open-circuit voltage of 0.61 V, and fill-factor of 65 leading to a power conversion efficiency of 4.64% at standard AM 1.5G solar light illumination.

Acknowledgments

The author T. Logu acknowledges Royal Society-SERB Newton International Fellowship (NIF\R1\192769). JK acknowledges financial support from the Department of Science and Technology, India, through the DST Inspire Faculty Award Grant (Grant No: DST/INSPIRE/04/2019/000283). JK thanks the Center for Computing and Information Sciences RGIPT-Jais for the high-performance computing facility.

Notes: The authors declare no competing financial interest.

Credit Author Statement

Logu Thirumalaisamy: Conceptualization, Methodology, Investigation, Formal analysis, Writing - Original Draft, Writing - Review & Editing

Soundarrajan Palanivel: Methodology, Validation, Writing - Review & Editing

Karthikeyan Jeyakumar: Methodology, Writing - Original Draft, Writing - Review & Editing

Sethuraman Kunjithapatham: Supervision, Resources, Validation, Writing - Review & Editing

Trystan Watson: Supervision, Investigation, Writing - Review & Editing

Sudhagar Pitchaimuthu: Supervision, Funding acquisition, Validation, Writing - Review & Editing

5 References

[1] H. Azimi, T. Heumüller, A. Gerl, G. Matt, P. Kubis, M. Distaso, R. Ahmad, T. Akdas, M. Richter, W. Peukert, C.J. Brabec, Relation of nanostructure and recombination dynamics in a low-temperature solution-processed CuInS2 nanocrystalline solar cell, Adv. Energy Mater. 3 (2013) 1589–1596. https://doi.org/10.1002/aenm.201300449.

[2] S. Siebentritt, Wide gap chalcopyrites: Material properties and solar cells, Thin Solid Films. 403–404 (2002) 1–8. https://doi.org/10.1016/S0040-6090(01)01525-5.

[3] B. Tell, J.L. Shay, H.M. Kasper, Room-Temperature Electrical Properties of Ten I-III-VI $_2$ Semiconductors, J. Appl. Phys. 43 (1972) 2469–2470. https://doi.org/10.1063/1.1661532.

[4] J. González-Hernández, P. Gorley, P.P. Horley, O.M. Vartsabyuk, Y.V. Vorobiev, X-Ray, kinetic and optical properties of thin CuInS2 films, Thin Solid Films. 403–404 (2002) 471–475. https://doi.org/10.1016/S0040-6090(01)01543-7.

[5] Q. Tian, G. Wang, W. Zhao, Y. Chen, Y. Yang, L. Huang, D. Pan, Versatile and low-toxic solution approach to binary, ternary, and quaternary metal sulfide thin films and its application in Cu 2ZnSn(S,Se)4 solar cells, Chem. Mater. 26 (2014) 3098–3103. https://doi.org/10.1021/cm5002412.

[6] S. Lei, C. Wang, L. Liu, D. Guo, C. Wang, Q. Tang, B. Cheng, Y. Xiao, L. Zhou, Spinel indium sulfide precursor for the phase-selective synthesis of Cu-In-S nanocrystals with zinc-blende, wurtzite, and spinel structures, Chem. Mater. 25 (2013) 2991–2997. https://doi.org/10.1021/cm400848f.

[7] T. Itsoponpan, C. Thanachayanont, P. Hasin, Sponge-like CuInS2 microspheres on reduced graphene oxide as an electrocatalyst to construct an immobilized acetylcholinesterase electrochemical biosensor for chlorpyrifos detection in vegetables, Sensors Actuators B Chem. 337 (2021) 129775. https://doi.org/10.1016/j.snb.2021.129775.

[8] J.J. Santaella, K. Critchley, S. Rodríguez-Bolívar, F.M. Gómez-Campos, Design and fabrication of CuInS2/ZnS-based QLED for automotive lighting systems,

Nanotechnology. 32 (2020). https://doi.org/10.1088/1361-6528/abcced.

[9] F. Yang, V. Kuznietsov, M. Lublow, C. Merschjann, A. Steigert, J. Klaer, A. Thomas, T. Schedel-Niedrig, Solar hydrogen evolution using metal-free photocatalytic polymeric carbon nitride/CuInS2 composites as photocathodes, J. Mater. Chem. A. 1 (2013) 6407–6415. https://doi.org/10.1039/c3ta10360a.

[10] K. Matoba, Y. Matsuda, M. Takahashi, Y. Sakata, J. Zhang, S. Higashimoto, Fabrication of Pt/In2S3/CuInS2 thin film as stable photoelectrode for water splitting under solar light irradiation, Catal. Today. 375 (2021) 87–93. https://doi.org/10.1016/j.cattod.2020.01.015.

[11] Y. Li, Z. Liu, Y. Wang, Z. Liu, J. Han, J. Ya, ZnO/CuInS2 core/shell heterojunction nanoarray for photoelectrochemical water splitting, Int. J. Hydrogen Energy. 37 (2012) 15029–15037. https://doi.org/10.1016/j.ijhydene.2012.07.117.

[12] T. Yukawa, K. Kuwabara, K. Koumoto, Electrodeposition of CulnS2 from aqueous solution (I I) Electrodeposifion of CuInS2 film, Thin Solid Films. 286 (1996) 151–153. https://doi.org/10.1016/S0040-6090(96)08545-8.

[13] R.P. Ankit Saneja1*, Chetan Sharma2, K.R. Aneja2, H.L. Hwang, C.L. Cheng, L.M. Liu, Y.C. Liu, C.Y. Sun, D. Perednis, L.J. Gauckler, S. Siebentritt, G.K. Williamson, R.E. Smallman, B. Tell, J.L. Shay, H.M. Kasper, F. Touhari, J. Bonnet, L. Lassabatere, N. Jebbari, N. Kamoun, R. Bennaceur, S. Belgacem, R.P.V. Lakshmi, R. Venugopal, D.R. Reddy, B.K. Reddy, T. Yamamoto, K. Fukuzaki, S. Kohiki, Z. Yan, W. Deng, X. Zhang, Q. Yuan, P. Deng, J. Liang, L. Sun, M. Ben Rabeh, N. Chaglabou, M. Kanzari, B. Rezig, G.T. Pan, M.H. Lai, R.C. Juang, T.W. Chung, T.C.K. Yang, J. Llanos, A. Buljan, C. Mujica, R. Ramfrez, F.M. Courtel, R.W. Paynter, B. Marsan, M. Morin, X. Sheng, L. Wang, L. Chang, Y. Luo, H. Zhang, J. Wang, D. Yang, P. Rajaram, R. Thangaraj, A.K. Sharma, A. Raza, O.P. Agnihotri, J. González-Hernández, P. Gorley, P.P. Horley, O.M. Vartsabyuk, Y.V. Vorobiev, K. Mori, M. Matsui, T. Watanabe, M. Ortega-López, A. Morales-Acevedo, T. Yukawa, K. Kuwabara, K. Koumoto, Characterization of CuInS2 thin films for solar cells prepared by spray pyrolysis, Thin Solid Films. 2 (2002) 345–349. https://doi.org/10.1021/cm900601k.

[14] C. Hubert, N. Naghavi, B. Canava, A. Etcheberry, D. Lincot, Thermodynamic and experimental study of chemical bath deposition of Zn(S,O,OH) buffer layers in basic aqueous ammonia solutions. Cell results with electrodeposited CuIn(S,Se)2 absorbers, Thin Solid Films. 515 (2007) 6032–6035. https://doi.org/10.1016/j.tsf.2006.12.139.

[15] W. Bensch, E. Quiroga-González, L. Kienle, V. Duppel, D.K. Lee, J. Janek, In-CuInS2 nanocomposite film prepared by pulsed laser deposition using a single source precursor, Solid State Sci. 12 (2010) 1953–1959. https://doi.org/10.1016/j.solidstatesciences.2010.08.005.

[16] K. Mori, M. Matsui, T. Watanabe, Thin film solar cells based on CuInS2 films through a two-stage process of sputtering and H2S annealing, Sol. Energy Mater. Sol. Cells. 35 (1994) 239–245. https://doi.org/10.1016/0927-0248(94)90146-5.

[17] K.R. Murali, A. Shanmugavel, K. Srinivasan, Photoelectrochemical characteristics of pulse electrodeposited CuInS2 films, Ionics (Kiel). 17 (2011) 157–162. https://doi.org/10.1007/s11581-010-0488-0.

[18] T. Logu, K. Sankarasubramanian, P. Soundarrajan, M. Sampath, K. Sethuraman, Growth of N type CuInS2 microspheres on P type CuInS2 seed layer prepared using facile low cost chemical methods, Superlattices Microstruct. 83 (2015) 690–698. https://doi.org/10.1016/j.spmi.2015.03.066.

[19] L. Thirumalaisamy, S. Palanivel, R. Raliya, S. Kavadiya, K. Sethuraman, P. Biswas, Single-step growth of CuInS2 nanospheres morphology thin films by electrospray chemical aerosol deposition technique, Mater. Lett. 238 (2019) 206–209. https://doi.org/10.1016/j.matlet.2018.12.021.

[20] X.H. Xu, F. Wang, J.J. Liu, K.C. Park, M. Fujishige, A novel one-step electrodeposition to prepare single-phase CuInS 2 thin films for solar cells, Sol. Energy Mater. Sol. Cells. 95 (2011) 791–796. https://doi.org/10.1016/j.solmat.2010.10.025.

[21] T. Logu, P. Soundarrajan, D. Naveena, K. Sankarasubramanian, S.M. Senthil Kumar, K. Sethuraman, Specific Al mole ratio doping aided flake-like ZnO surface morphology nanostructures film for efficient window layer in CuInS2 photovoltaic cells, Sol. Energy.

177 (2019) 108–117. https://doi.org/10.1016/j.solener.2018.11.006.

[22] J. van Embden, J.O. Mendes, J.J. Jasieniak, A.S.R. Chesman, E. Della Gaspera, Solution-Processed CuSbS 2 Thin Films and Superstrate Solar Cells with CdS/In 2 S 3 Buffer Layers, ACS Appl. Energy Mater. 3 (2020) 7885–7895. https://doi.org/10.1021/acsaem.0c01296.

[23] D. Naveena, L. Thirumalaisamy, R. Dhanabal, K. Sethuraman, A.C. Bose, Tuning the Properties of the CuAl (1– X) Fe X S 2 Thin Film as a Potential Absorber for Solar Cell Application, ACS Appl. Energy Mater. 3 (2020) 10550–10559. https://doi.org/10.1021/acsaem.0c01608.

[24] T. Logu, K. Sankarasubramanian, P. Soundarrajan, J. Archana, Y. Hayakawa, K. Sethuraman, Vanadium doping induces surface morphological changes of CuInS2 thin films deposited by chemical spray pyrolysis, J. Anal. Appl. Pyrolysis. 122 (2016) 230–240. https://doi.org/10.1016/j.jaap.2016.09.019.

[25] T. Logu, K. Sankarasubramanian, P. Soundarrajan, K. Ramamurthi, K. Sethuraman, Materials design of n-type CuInS2 thin films with reduction of Cu–Au phase using Cd2+ ions, J. Anal. Appl. Pyrolysis. 114 (2015) 293–301. https://doi.org/10.1016/j.jaap.2015.06.011.

[26] L. Thirumalaisamy, R. Raliya, S. Kavadiya, S. Palanivel, K. Sethuraman, P. Biswas, Hierarchical architecture of CuInS 2 microsphere thin films: altering laterally aligned crystallographic plane growth by Cd and V doping, CrystEngComm. 19 (2017) 6602–6611. https://doi.org/10.1039/C7CE01293D.

[27] N.K. Allouche, N. Jebbari, C. Guasch, N.K. Turki, Influence of aluminum doping in CuInS2 prepared by spray pyrolysis on different substrates, J. Alloys Compd. 501 (2010) 85–88. https://doi.org/10.1016/j.jallcom.2010.04.041.

[28] T. Yamamoto, T. Negami, K. Matsubara, S. Niki, Fabrication and characterization of wide-gap ZnCuInS 2 solar cells, Jpn. J. Appl. Phys. 51 (2012) 1–4. https://doi.org/10.1143/JJAP.51.10NC06.

[29] C. Mahendran, N. Suriyanarayanan, Influence of mole concentration on nano crystalline Bi-doped CuInS2 thin films with the temperature by chemical spray method, Optik (Stuttg). 126 (2015) 4237–4242. https://doi.org/10.1016/j.ijleo.2015.08.133.

[30] M. Ben Rabeh, N. Chaglabou, M. Kanzari, B. Rezig, Structural and optical studies on antimony and zinc doped CuInS2 thin films, Phys. Procedia. 2 (2009) 745–750. https://doi.org/10.1016/j.phpro.2009.11.020.

[31] T. Logu, P. Soundarrajan, R.H. Ramprasath, K. Sethuraman, Highly crystalline and improved photo-response property of CuInS2 thin films via Yb doping by chemical spray pyrolysis technique, in: AIP Conf. Proc., 2019: p. 030320. https://doi.org/10.1063/1.5113159.

[32] Z.-X. He, H. Yu, F. He, Y. Xie, L. Yuan, T. Yi, Effects of Ru doping on the structural stability and electrochemical properties of Li 2 MoO 3 cathode materials for Li-ion batteries, Dalt. Trans. 51 (2022) 8786–8794. https://doi.org/10.1039/D2DT00826B.

[33] L. Malavasi, M.C. Mozzati, C. Tealdi, C.B. Azzoni, G. Flor, Influence of Ru doping on the structure, defect chemistry, magnetic interaction, and carrier motion of the la1-xNaxMnO 3+δ manganite, J. Phys. Chem. B. 109 (2005) 20707–20713. https://doi.org/10.1021/jp052423z.

[34] W. Chen, J. Qi, C. Dong, J. Chen, Z. Shen, Y. He, S. Yang, T. Chen, C. Chen, Y. Li, M.-D. Li, M. Wang, Solution-Processed in Situ Growth of CuInS 2 Nanoparticle Films for Efficient Planar Heterojunction Solar Cells with a Dual Nature of Charge Generation, ACS Appl. Energy Mater. 2 (2019) 5231–5242. https://doi.org/10.1021/acsaem.9b00915.

[35] S.S. Viveka, T. Logu, N. Ahsan, J. Karthikeyan, P. Murugan, M. Sampath, S. Kalainathan, A. Gupta, Y. Okada, K. Sethuraman, Fe-doped CuGaS2 (CuGa1-xFexS2) - Detailed analysis of the intermediate band optical response of chalcopyrite thin films based on first principle calculations and experimental studies, Mater. Sci. Semicond. Process. 136 (2021) 106133. https://doi.org/10.1016/j.mssp.2021.106133.

[36] T. Logu, K. Sankarasubramanian, P. Soundarrajan, K. Sethuraman, Growth of CuInS2 microspheres on CuInS2 seed layer prepared using facile low cost chemical methods, in:

2015: p. 080066. https://doi.org/10.1063/1.4917970.

[37] G.K. Williamson, R.E. Smallman, III. Dislocation densities in some annealed and cold-worked metals from measurements on the X-ray debye-scherrer spectrum, Philos. Mag. 1 (1956) 34–46. https://doi.org/10.1080/14786435608238074.

[38] T. Schwarz, A. Lomuscio, S. Siebentritt, B. Gault, On the chemistry of grain boundaries in CuInS2 films, Nano Energy. 76 (2020). https://doi.org/10.1016/j.nanoen.2020.105081.

[39] S.S. Viveka, T. Logu, N. Ahsan, K. Asokan, S. Kalainathan, K. Sethuraman, Y. Okada, Study of sub-band states formation in the optical band gap of CuGaS2 thin films by electronic excitations, J. Phys. Chem. Solids. 164 (2022) 110636. https://doi.org/10.1016/j.jpcs.2022.110636.

[40] C. Mahendran, N. Suriyanarayanan, Effect of zinc doping and temperature on the properties of sprayed CuInS2 thin films, Mater. Sci. Semicond. Process. 15 (2012) 522–530. https://doi.org/10.1016/j.mssp.2012.04.001.

[41] J.J. Frick, G. Cheng, S. Kushwaha, N. Yao, S. Wagner, A.B. Bocarsly, R.J. Cava, Observation of [V Cu 1– In i 2+ V Cu 1–] Defect Triplets in Cu-Deficient CuInS 2, J. Phys. Chem. C. 124 (2020) 26415–26427. https://doi.org/10.1021/acs.jpcc.0c08872.

[42] L. Thirumalaisamy, N. Ahsan, K. Sivaperuman, M. Kim, S. Kunjithapatham, Y. Okada, Engineering of sub-band in CuGaS2 thin films via Mo doping by chemical spray pyrolysis route, Thin Solid Films. 709 (2020) 138252. https://doi.org/10.1016/j.tsf.2020.138252.

[43] F.M. Courtel, R.W. Paynter, B. Marsan, M. Morin, Synthesis, Characterization, and Growth Mechanism of n-Type CuInS $_2$ Colloidal Particles, Chem. Mater. 21 (2009) 3752–3762. https://doi.org/10.1021/cm900601k.

[44] T. Logu, P. Soundarrajan, K. Sankarasubramanian, K. Sethuraman, Enhanced photo response of mesoporous nanostructured CdS thin film via electrospray aerosol deposition technique, in: AIP Conf. Proc., 2018: p. 080066. https://doi.org/10.1063/1.5028900.

[45] S. Sarkar, K. Bhattacharjee, G.C. Das, K.K. Chattopadhyay, B. Ananthoju, A. Kushwaha, F.J. Sonia, M. Aslam, Self-sacrificial template directed hydrothermal route to kesterite-Cu

<inf>2</inf>ZnSnS<inf>4</inf> microspheres and study of their photo response properties, AIP Conf. Proc. 1512 (2013) 706–707. https://doi.org/10.1039/c3ce42229a.

[46] M. Sampath, T. Logu, P. Mathan Kumar, K. Asokan, K. Sethuraman, Enhancement of photoelectric properties of Cu2ZnSnS4 thin films by electronic excitations induced by swift heavy ions, Mater. Sci. Eng. B. 280 (2022) 115683. https://doi.org/10.1016/j.mseb.2022.115683.

[47] S. Kalainathan, N. Ahsan, T. Hoshii, Y. Okada, T. Logu, K. Sethuraman, Tailoring sub-bandgap of CuGaS2 thin film via chromium doping by facile chemical spray pyrolysis technique, J. Mater. Sci. Mater. Electron. 29 (2018) 19359–19367. https://doi.org/10.1007/s10854-018-0065-2.

[48] E. Kärber, A. Abass, S. Khelifi, M. Burgelman, A. Katerski, M. Krunks, Electrical characterization of all-layers-sprayed solar cell based on ZnO nanorods and extremely thin CIS absorber, Sol. Energy. 91 (2013) 48–58. https://doi.org/10.1016/j.solener.2013.01.020.

[49] T. Ryo, D.C. Nguyen, M. Nakagiri, N. Toyoda, H. Matsuyoshi, S. Ito, Characterization of superstrate type CuInS2 solar cells deposited by spray pyrolysis method, Thin Solid Films. 519 (2011) 7184–7188. https://doi.org/10.1016/j.tsf.2010.12.176.

[50] A.H. Cheshme khavar, A. Mahjoub, F.S. Samghabadi, N. Taghavinia, Fabrication of selenization-free superstrate-type CuInS2 solar cells based on all-spin-coated layers, Mater. Chem. Phys. 186 (2017) 446–455. https://doi.org/10.1016/j.matchemphys.2016.11.017.

[51] M. Esmaeili-Zare, M. Behpour, Influence of deposition parameters on surface morphology and application of CuInS2 thin films in solar cell and photocatalysis, Int. J. Hydrogen Energy. 45 (2020) 16169–16182. https://doi.org/10.1016/j.ijhydene.2020.04.106.

[52] M. Dehghani, E. Parvazian, N.A. Tehrani, N. Taghavinia, M. Samadpour, A novel low-temperature growth of uniform CuInS2 thin films and their application in selenization/sulfurization-free CuInS2 solar cells, Mater. Today Commun. 26 (2021) 102050. https://doi.org/10.1016/j.mtcomm.2021.102050.

[53] W. Chen, W. Cao, R. Liu, C. Dong, Z. Wan, J. Chen, G.Y. Ashebir, M. Wang, Solution-Processed All-inorganic Planar Heterojunction Solar Cells by Employing in Situ Grown Interfacial Layer with Dual Functions: Complementary Absorption and Selective Extraction of Photogenerated Holes, ACS Omega. 6 (2021) 6973–6980. https://doi.org/10.1021/acsomega.0c06231.

[54] D. Lee, K. Yong, Superstrate CuInS2 photovoltaics with enhanced performance using a CdS/ZnO nanorod array, ACS Appl. Mater. Interfaces. 4 (2012) 6758–6765. https://doi.org/10.1021/am301957d.

[55] A.H. Cheshme Khavar, A.R. Mahjoub, H. Fakhri, Controlled Synthesis of Nanostructured CuInS2: Study of Mechanism and Its Application in Low-Cost Solar Cells, J. Inorg. Organomet. Polym. Mater. 26 (2016) 1075–1086. https://doi.org/10.1007/s10904-016-0417-4.

[56] Y. Di Iorio, M. Berruet, D.L. Gau, E.L. Spera, C.J. Pereyra, R.E. Marotti, M. Vázquez, Efficiency Improvements in Solution-Based CuInS2 Solar Cells Incorporating a Cl-Doped ZnO Nanopillars Array, Phys. Status Solidi Appl. Mater. Sci. 214 (2017) 1–8. https://doi.org/10.1002/pssa.201700191.

[57] Y. Tani, K. Imada, T. Kamimura, M. Takahashi, M. Anpo, S. Higashimoto, Solution-processed fabrication of copper indium sulfide (CuInS2) as optical absorber for superstrate CuInS2/CdS/TiO2 solid-state solar cells, Res. Chem. Intermed. 47 (2021) 169–182. https://doi.org/10.1007/s11164-020-04349-8.

[58] W. Xia, C. Mei, X. Zeng, S. Chang, G. Wu, X. Shen, Mesoporous multi-shelled ZnO microspheres for the scattering layer of dye sensitized solar cell with a high efficiency, Appl. Phys. Lett. 108 (2016). https://doi.org/10.1063/1.4944532.